Molecular insights into lipid-assisted Ca^{2+} regulation of the TRP channel Polycystin-2

Martin Wilkes[1], M Gregor Madej[2], Lydia Kreuter[2,6], Daniel Rhinow[1], Veronika Heinz[2], Silvia De Sanctis[2], Sabine Ruppel[2], Rebecca M Richter[2], Friederike Joos[1], Marina Grieben[3], Ashley C W Pike[3], Juha T Huiskonen[4], Elisabeth P Carpenter[3], Werner Kühlbrandt[1], Ralph Witzgall[5] & Christine Ziegler[2]

Polycystin-2 (PC2), a calcium-activated cation TRP channel, is involved in diverse Ca^{2+} signaling pathways. Malfunctioning Ca^{2+} regulation in PC2 causes autosomal-dominant polycystic kidney disease. Here we report two cryo-EM structures of distinct channel states of full-length human PC2 in complex with lipids and cations. The structures reveal conformational differences in the selectivity filter and in the large exoplasmic domain (TOP domain), which displays differing N-glycosylation. The more open structure has one cation bound below the selectivity filter (single-ion mode, PC2$_{SI}$), whereas multiple cations are bound along the translocation pathway in the second structure (multi-ion mode, PC2$_{MI}$). Ca^{2+} binding at the entrance of the selectivity filter suggests Ca^{2+} blockage in PC2$_{MI}$, and we observed density for the Ca^{2+}-sensing C-terminal EF hand in the unblocked PC2$_{SI}$ state. The states show altered interactions of lipids with the pore loop and TOP domain, thus reflecting the functional diversity of PC2 at different locations, owing to different membrane compositions.

Cytoplasmic Ca^{2+} concentrations are spatially and temporally regulated by a finely balanced interplay between active Ca^{2+} export and Ca^{2+} influx through Ca^{2+}-sensitive channels[1]. The transient receptor potential (TRP) channel PC2 (ref. 2) is a nonselective cation channel that participates in a variety of different Ca^{2+}-dependent signaling pathways including the Wnt pathway[2,3]. PC2 is found in the endoplasmic reticulum (ER)[4,5], the primary cilia[6,7] and the plasma membrane[6,8], and its subcellular distribution varies greatly among different cell types. Single-channel studies have indicated that PC2 conducts monovalent and divalent ions including Ca^{2+} (refs. 9–11). In the ER, PC2 has also been reported to act as a Ca^{2+}-activated Ca^{2+}-release channel[11,12]. Different experimental approaches have suggested that PC2 also indirectly modulates the cytosolic calcium concentration by interacting with key proteins involved in Ca^{2+} import[13], including TRPV4, TRPC1 (ref. 14) and TRPC4 at the ciliary or somatic membrane[15–17]. In the ER, PC2 modulates calcium release through interaction with the inositol 1,4,5-triphosphate receptor (IP$_3$R)[13] or with the ryanodine receptor RyR[12]. The most prominent interaction partner of PC2 is Polycystin-1 (PC1)[18,19], a channel-like receptor that competitively mediates PC2 complex formation[18–20]. Mutations in PC2 or PC1 that affect their mutual interaction are among the factors causing autosomal-dominant polycystic kidney disease (ADPKD)[2,21].

Trafficking of PC2 is controlled through a set of specific N- and C-terminal sequences and is dependent on the availability of a variety of interaction partners[12,13,16]. An N-terminal R$_6$VXP motif is required for relocation of PC2 to primary cilia[22]. N-glycosylation in the exoplasmic domain of loop 1 between the first and second transmembrane helices is essential for trafficking of PC2 to the Golgi apparatus and beyond[23]. Retention of PC2 in the early secretory pathway involves an ER-retention signal[5], which is located in the C-terminal domain[5], adjacent to a downstream Ca^{2+}-binding EF-hand motif[24] and coiled-coil helices. Whereas the coiled-coil regions are instrumental in complex formation and hetero-oligomerization[4,18,19,25,26], the conformation of the EF-hand motif is essential for opening of the full-length PC2 and thus for Ca^{2+} activation. The open probability of PC2 is bell shaped at free-Ca^{2+} concentrations between ~10 nM and ~1 mM (ref. 27). Although the activation at low Ca^{2+} concentrations can be assigned to the Ca^{2+}-sensing EF hand, the reason for inactivation at high Ca^{2+} concentrations is largely unknown[28].

Until recently, no structures have been available for the membrane-embedded part of the channel. Grieben *et al.*[29] have reported a cryo-EM structure of a terminal truncated construct, solved in combination with X-ray crystallography data, that reveals a closed state, which we refer to as PC2$_{CL}$. Shen *et al.*[30] have reported another cryo-EM structure of an N- and C-terminally truncated PC2 construct reconstituted into nanodiscs. Here we present two structures of full-length human PC2 in different conformational states at 4.2-Å and 4.3-Å resolution, as determined by cryo-EM with the PC2$_{CL}$ structure as the initial model. The two states are open at the selectivity filter and are in complex with lipids and cations, neither of which is present in PC2$_{CL}$. The conformational differences between the two states provide initial insights into a blocking mechanism causing PC2

inactivation at high Ca^{2+} concentrations and highlight the effect of membrane composition on PC2 function.

RESULTS

Single-particle cryo-EM of two PC2 forms

Full-length PC2 was overexpressed in HEK293 GnTI⁻ cells[31] (**Supplementary Fig. 1a,b**). At 2 to 3 d after induction, we observed the formation of massively enlarged and highly vesiculated ER membranes, known as crystalloid ER, by electron microscopy of thin plastic sections (**Supplementary Fig. 1c**). Focused ion-beam milling SEM (FIB-SEM)[32] revealed that the crystalloid ER is a network of elongated tubes (**Supplementary Fig. 1d**). Immunogold labeling of thin plastic sections indicated that the majority of PC2 was in the ER, although some PC2 was also present in the plasma membrane (**Supplementary Fig. 1e**). We purified PC2 through Strep-II-tag affinity chromatography and reconstituted it in amphipols A8-35. Western blot analysis, MS–MS and treatment with PNGase F confirmed the presence of full-length, N-glycosylated PC2, which we investigated by single-particle cryo-EM (**Supplementary Fig. 2**). 3D classification of the cryo-EM data set revealed two distinct conformational states of PC2 that were present in approximately equally proportions (**Supplementary Fig. 3**). We performed homology-model-guided *de novo* building of the transmembrane region. Unlike the TRPV and TRPA channels[33–35], PC2 has a large exoplasmic insertion between S1 and S2 in loop 1: the tetragonal opening for polycystin (TOP) domain. Our initial attempts to resolve
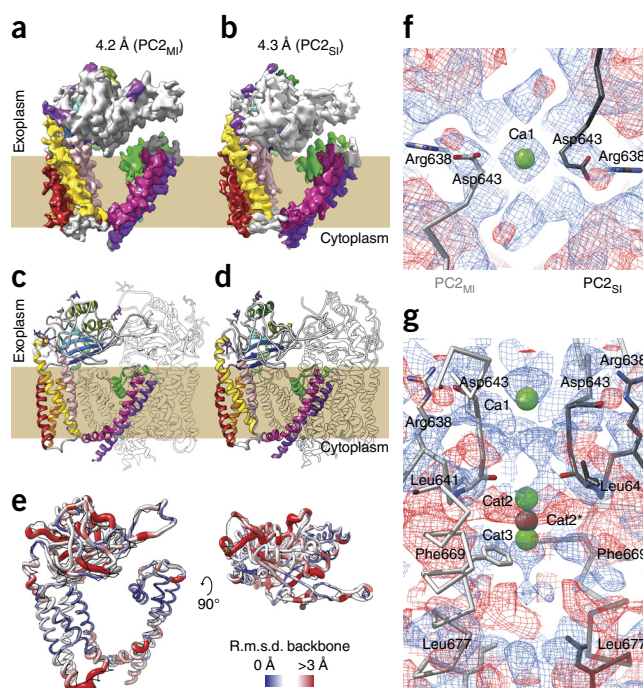
Table 1 Cryo-EM data, refinement and model statistics

	PC2$_{SI}$ (EMD-3523, PDB 5MKE)	PC2$_{MI}$ (EMD-3524, PDB 5MKF)
Data collection		
Microscope	JEOL 3200FSC	JEOL 3200FSC
Voltage (kV)	300	300
Defocus range (µm)	0.5–4.0	0.5–4.0
Pixel size (Å)	1.14	1.14
Average e⁻ dose per image (e⁻/Å²)	1.8	1.8
Particles (initial)	267,010	267,010
Particles (final (%))	42,268 (16)	35,318 (13)
Reconstruction		
Symmetry	$C4$	$C4$
Resolution (unmasked; Å)	4.5	4.5
Resolution (masked; Å)	4.3	4.2
Map-sharpening B factor (Å²)	−200	−200
Model composition		
Nonhydrogen atoms	15,704	15,848
Protein residues	1,900	1,924
Nonprotein residues	36	36
Refinement		
Resolution (Å)	4.3	4.2
Map-sharpening B factor (Å²)	−105	−95
Model-to-map fit (CC)	0.6924	0.7203
R.m.s. deviations		
Bonds (Å)	0.009	0.009
Angles (°)	1.155	1.091
Validation		
Clashscore	48.28	31.05
Rotamer outliers (%)	0.23	0.23
Ramachandran plot (% favored)	91.30	93.32
Ramachandran plot (% outliers)	0.21	0

Figure 1 Segmented map volumes showing PC2 protomers of the 4.2-Å-resolution structure (PC2$_{MI}$) and the 4.3-Å-resolution structure (PC2$_{SI}$). (**a,b**) Maps of PC2$_{MI}$ (**a**) and PC2$_{SI}$ (**b**) showing the transmembrane helices S1 (orange), S2 (red), S3 (yellow) and S4 (mauve); the pore helices S5 (magenta), S6 (purple); and the P loop with two segments of a helix hairpin (PH1 and PH2, green). (**c,d**) Secondary-structure models of PC2$_{MI}$ (**c**) and PC2$_{SI}$ (**d**). Transmembrane helices are colored as in **a**; the three α-helices and five β-sheets of the TOP domain are shown in different shades of green and blue; the loops are gray. Neighboring protomers are indicated as blank silhouettes. (**e**) Structural differences between PC2$_{MI}$ and PC2$_{SI}$. PC2$_{MI}$ is shown as a tube model; the Cα r.m.s. deviation (r.m.s.d.) is indicated by the color and radius of the tubes (blue, >0 Å; white, ~1.5 Å; red, >3 Å) in superposition with PC2$_{SI}$ (black wire). The tetrameric PC2 with densities in the translocation pathway are shown in **Figure 3**. (**f,g**) Top (**f**) and side (**g**) views of a difference map between PC2$_{MI}$ and PC2$_{SI}$ (mesh at the 4σ contour level; blue indicates positive difference density, and red indicates negative difference density). Structure models for PC2$_{MI}$ (left) and PC2$_{SI}$ (right) are shown in complex with cations (green spheres in PC2$_{MI}$ or gray sphere in PC2$_{SI}$).

the structure of the TOP domain were unsuccessful until we compared the electron density with that of the PC2$_{CL}$ structure[29], at which point it became clear that the two 3D classes represented two different channel conformations. When we merged data sets from both 3D classes, the resulting map was ambiguous and could not be modeled with an acceptable number of backbone dihedral-angle outliers, even though the nominal resolution was 3.9 Å, owing to the two-fold-larger number of particles. Individual processing of both forms resulted in two maps with overall resolutions of 4.2 Å and 4.3 Å, respectively (**Fig. 1a–d** and **Supplementary Fig. 4**). Differences between the two maps were clearly visible at a high sigma level of 4 (**Fig. 1f,g**). We refined the models by using phenix.real_space_refine[36] and the Rosetta[37] toolbox for structure determination on the basis of the cryo-EM densities. The structures show the six transmembrane (TM) helices, the TOP domain and the pore (**Fig. 1c–e** and **Table 1**). Although we obtained both structures from the full-length construct, the N- and C-terminal domain were not resolved at the atomic level. We observed cytoplasmic densities only in the 4.3-Å-resolution map. The well-resolved map regions corresponded to those of the truncated PC2$_{CL}$ structure[29].
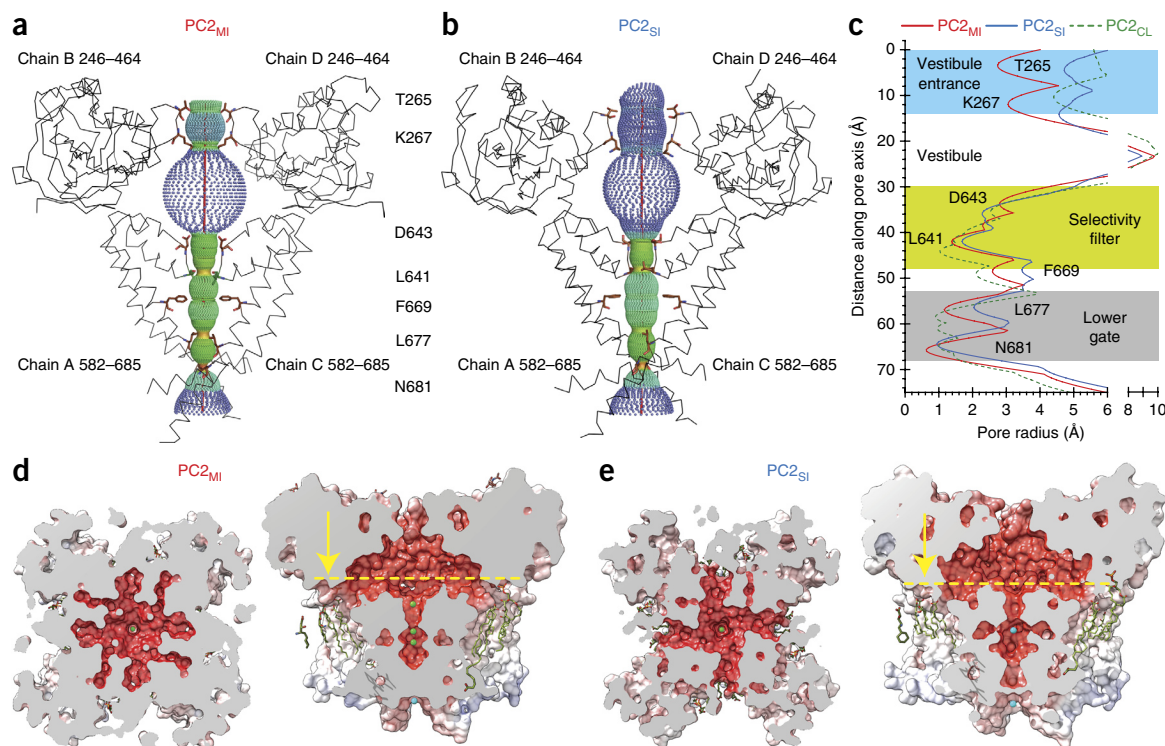
Figure 2 Ion-translocation pathway in $PC2_{MI}$ and $PC2_{SI}$. (**a,b**) Profiles of the $PC2_{MI}$ translocation pathway (**a**) and the $PC2_{SI}$ translocation pathway (**b**), shown as the radius along the pathway, generated with the script HOLE. Parts of $PC2_{MI}$ and $PC2_{SI}$ Cα traces are shown as black wire for orientation. The conformations of T265, K267, D643, L641, F669, L677 and N681 along the pathway constrain the ion-translocation pathway, which is less restricted in $PC2_{SI}$ than in $PC2_{MI}$. (**c**) Radius of the translocation pathway for both PC2 forms in comparison to the closed form ($PC2_{CL}$, c.f. Grieben *et al.*[29]). Constricting residues are indicated. (**d,e**) Sagittal slice through the electrostatic surface representation of $PC2_{MI}$ (**d**) and $PC2_{SI}$ (**e**). The vestibule formed by the TOP domains is highly negatively charged (red). Exit funnels in both structures are located at different positions (yellow arrows). Ca^{2+} and other cations are shown as green and blue spheres (see also **Fig. 3c,d**).

In contrast to the results for $PC2_{CL}$, several spherical nonprotein densities are visible in the ion-translocation pathway of both maps, at intensities comparable to those of the protein densities, thus suggesting the presence of cations in the pore. The difference map reveals densities in the 4.2-Å-resolution map above and below the selectivity filter, whereas only one such density is visible below the selectivity filter in the 4.3-Å-resolution map (**Fig. 1g**). Additional densities are present in both maps at the cytoplasmic exit of the channel. In the following discussion, we refer to the two PC2 structures reported here as the multi-ion state, or $PC2_{MI}$, which was obtained from the 4.2-Å-resolution map, and the single-ion state or $PC2_{SI}$, which was obtained from the 4.3-Å-resolution map.

The two full-length PC2 structures as well as $PC2_{CL}$ exhibit the characteristic TRP-channel architecture of six transmembrane helices (S1–S6) and a hairpin loop (P loop) between S5 and S6 (**Fig. 1c,d**). In the PC2 tetramer, the selectivity filter is lined by Asp643, Gly642 and Leu641, which, together with residues in S6, form the ion-translocation pathway of PC2 (**Fig. 2a–c**). The unique fold of the TOP domain comprises three α-helices, five β-sheets and their intervening loops, EL1–EL3 (**Fig. 1c,d**), and its structure has been described in detail in Grieben *et al.*[29].

$PC2_{MI}$ and $PC2_{SI}$ deviate from each other in several regions of the TOP domain; in loop 2 between S2 and S3; in the linker between S4 and S5; in the cytoplasmic ends of S5 and S6 and in the region of the P loop that connects PH1 and PH2 to S5 and S6 (P-loop junctions) (**Fig. 1e**). The $PC2_{MI}$ and $PC2_{SI}$ states differ from the $PC2_{CL}$ state reported in Grieben *et al.*[29], with regard to the

orientation of the TOP domain and the S1–S2 and S5–S6 regions (**Supplementary Fig. 5c,d**).

Cation-binding sites in PC2

$PC2_{MI}$ and $PC2_{SI}$ are considerably more open than $PC2_{CL}$ at the selectivity filter and the lower gates (**Fig. 2c**), and several spherical densities are present in the ion pathway. However, $PC2_{MI}$ shows a restriction that is located at Asn681 and is less pronounced in $PC2_{SI}$ and $PC2_{CL}$.

On the basis of coordination geometry and comparison with the X-ray structures of Ca_VAB (PDB 4MVO)[38] (**Supplementary Fig. 5a**) and TRPV6 (PDB 5IWK)[35], the nonprotein density at the entrance of the selectivity filter of the $PC2_{MI}$ tetramer (**Fig. 3a,b**) may represent a hydrated Ca^{2+} ion (Ca1) because 2 mM Ca^{2+} was present throughout purification. Ca1 is coordinated by a planar arrangement of four Asp643 carboxyls (**Fig. 3c,d**). However, given that PC2 is believed to be nonselective for cations, the remaining spherical densities (Cat2–Cat4), which lack clear coordination, might represent monovalent ions such as sodium, which was present at a concentration of 75 mM throughout the purification and cryopreservation. Nevertheless, Cat2 and Cat3 are present at positions analogous to the Ca^{2+}-binding sites in Ca_VAB[38], which also shows a restriction at a position analogous to that of Asn681. Given the higher concentration and similar permeability of Na^+ ions, it is possible that Na^+, rather than Ca^{2+} ions are bound in some of the sites in the ion pathway. Potassium ions were not present in the buffer, so it is unlikely that there are K^+ ions bound in these sites in the structure, but it is possible that K^+ ions may occupy
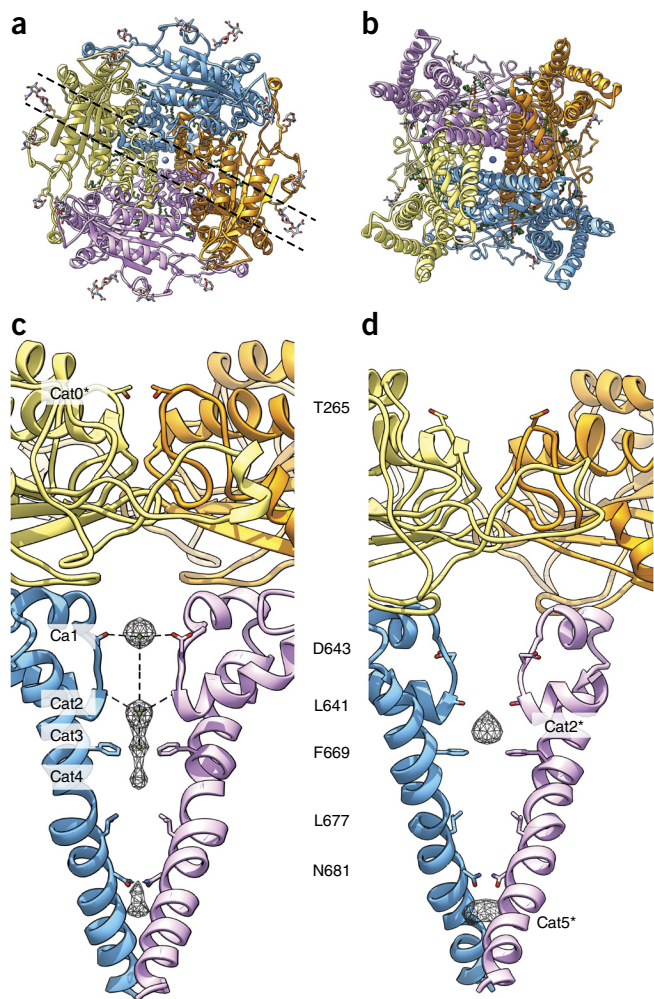
Figure 3 Cation-binding sites in PC2. (**a**) Top view of the PC2$_{MI}$ tetramer. Each protomer is in a different color; cations are shown as spheres. Broken lines indicate the approximate viewing direction in **c**. (**b**) Cytoplasmic view of the PC2$_{MI}$ tetramer; color-coded as in **a**. (**c**) Cations along the translocation pathway in PC2$_{MI}$. Isolated densities (2σ) along the translocation pathway are shown as black mesh. Positions overlapping with Ca^{2+}-binding sites in Ca$_V$AB and TRPV6 are indicated with green spheres (see also **Supplementary Fig. 5a**), and several prominent side chains are shown. (**d**) Isolated densities (2σ) along the translocation pathway in PC2$_{SI}$ are shown as black mesh. Positions Cat2* and Cat5* are close but not identical to Cat2 and Cat5. The protein and several prominent side chains are color-coded as in **a**.

these sites in the cell. The four backbone carbonyl oxygens of Leu641 are able to coordinate a cation, such as Ca^{2+} or Na$^+$, in the Ca2 site just below the selectivity filter.

The selectivity filter is more open in PC2$_{SI}$, having a pore radius of 1.7 Å at Leu641, as determined in HOLE, compared with 1.4 Å in PC2$_{MI}$ and 1.0 Å in PC2$_{CL}$. We observed changes in the conformation of Asp643, a residue previously described as a water stripper in PC2 (ref. 28). Its interaction with Arg638, which contributes to the architecture of the P loop, is altered and affects the pore radius (**Fig. 1g**). Moreover, the Ca1 site, which is thought to be a high-affinity site in Ca$_V$AB[38] and TRPV6 (ref. 35) (**Supplementary Fig. 5a**), is not formed in PC2$_{SI}$. Comparison of both open structures indicates that the most likely interpretation is that only PC2$_{MI}$ represents a state in which Ca^{2+} is bound to the Ca1 site. The environments of the Cat3 and Cat4 sites in PC2$_{MI}$ are hydrophobic and cannot be unambiguously

assigned as Ca^{2+}-binding sites. Similarly, the elongated density below the Cat2* site in PC2$_{SI}$ (**Fig. 3d**) can accommodate two cations, one of which would be coordinated in the selectivity filter by the four backbone carbonyl oxygens of Leu641.

Phe669, between the Cat3 and Cat4 sites, restricts the channel diameter. In Ca$_V$AB, fatty acid chains participate in an even tighter channel constriction at this point (**Supplementary Fig. 5b**). At the channel exit, Asn681 and Ser685 coordinate a spherical density at the Cat5 site (**Fig. 3**) in PC2$_{MI}$ and PC2$_{SI}$.

α1, EL1, α2 and β5 in the TOP domain form a spacious, negatively charged vestibule. PC2$_{MI}$ shows a confined entrance gate from the exoplasmic side of the membrane at Thr265 and Lys267 (Cat0; **Figs. 2c** and **3**). At its narrowest point, the vestibule entrance has a radius of 3.0 Å in PC2$_{MI}$, whereas it is open in PC2$_{SI}$ and PC2$_{CL}$, which have radii of 4.7 Å and 4.4 Å, respectively. Thus, PC2$_{MI}$ serves as a preselectivity filter in which access of hydrated ions such as Ca^{2+}, Na$^+$ and K$^+$, which have radii of 4.1 Å, 3.6 Å and 3.3 Å, respectively, would be restricted, but the passage of dehydrated ions would be permitted.

Differing N-glycosylation in PC2$_{MI}$ and PC2$_{SI}$

The five potential N-glycosylation sites[23] Asn299, Asn305, Asn328, Asn362 and Asn375 are all located in EL2 or EL3. Four of five asparagine residues are N-glycosylated in PC2$_{MI}$ (Asn299 in EL2; Asn328, Asn362 and Asn375 in EL3), and they contribute to the well-ordered loop regions (**Fig. 1c,d** and **Fig. 4**). A disulfide bridge between Cys331 and Cys344 plus a helix segment at Gln335–Glu340 stabilize EL3, thus enabling its interaction with the hairpin in loop 3 of the neighboring protomer (**Fig. 4a**). This disulfide bridge is also not seen in PC2$_{CL}$ and in PC2$_{SI}$, although PC2$_{CL}$ is generally more similar to PC2$_{MI}$ than to PC2$_{SI}$. In PC2$_{SI}$, Asn305, Asn362 and Asn375 are N-glycosylated, but Asn328 is not (**Fig. 4b**). The nonglycosylated asparagine interacts with Glu343. From the comparison with PC2$_{SI}$, it can be inferred that a bulky glycan group at Asn305 would prevent the intratetramer interactions of loop 3, as observed in PC2$_{MI}$. Loop 3 in PC2$_{SI}$ instead interacts with EL2 in the same protomer, thus accounting for the partly disordered TOP domain.

The conformational changes in the TOP domains of the two structures are associated with differing patterns of N-glycosylation. N-glycosylation of Asn305 and Asn328 are mutually exclusive: if one residue is glycosylated, the other is not. One possible explanation is that N-glycosylation of one site renders the other site inaccessible to glycosylation. Whether N-glycosylation triggers the conformational changes between PC2$_{MI}$ and PC2$_{SI}$ or whether the differing states might dictate the differing N-glycosylation patterns remain intriguing questions. Differences in N-glycosylation affect the conformation of β5 and the position of α1 (**Fig. 4c,d**). Most interactions of the TOP domain with the P loop of the neighboring protomer are substantially different in PC2$_{MI}$ and PC2$_{SI}$ (**Fig. 4c,d**). In PC2$_{MI}$, Glu651 is in contact with Trp455 in β5, and Gln456 is in contact with Gln622 of PH1. In PC2$_{SI}$, Gln622 interacts with Ser254 in α1, and Glu651 in PH2 interacts with the TOP domain via Lys271. Gln622, Glu651 and Asn653 in the P-loop joints act as anchor points. PH1 and PH2 move closer in PC2$_{MI}$ (**Fig. 4c**) than in PC2$_{SI}$ (**Fig. 4d**), thereby switching the interaction between Asp643 and Arg638 in the selectivity filter (**Fig. 1f,g**).

Lipid coordination in PC2

Both maps show a number of elongated densities in the hydrophobic cleft between S4 of one protomer and S5 and S6 of the next protomer (**Fig. 5a**). We attribute three of these densities to single-chain fatty acids. Two fatty acid chains (FA1 and FA2) belong to the outer-membrane
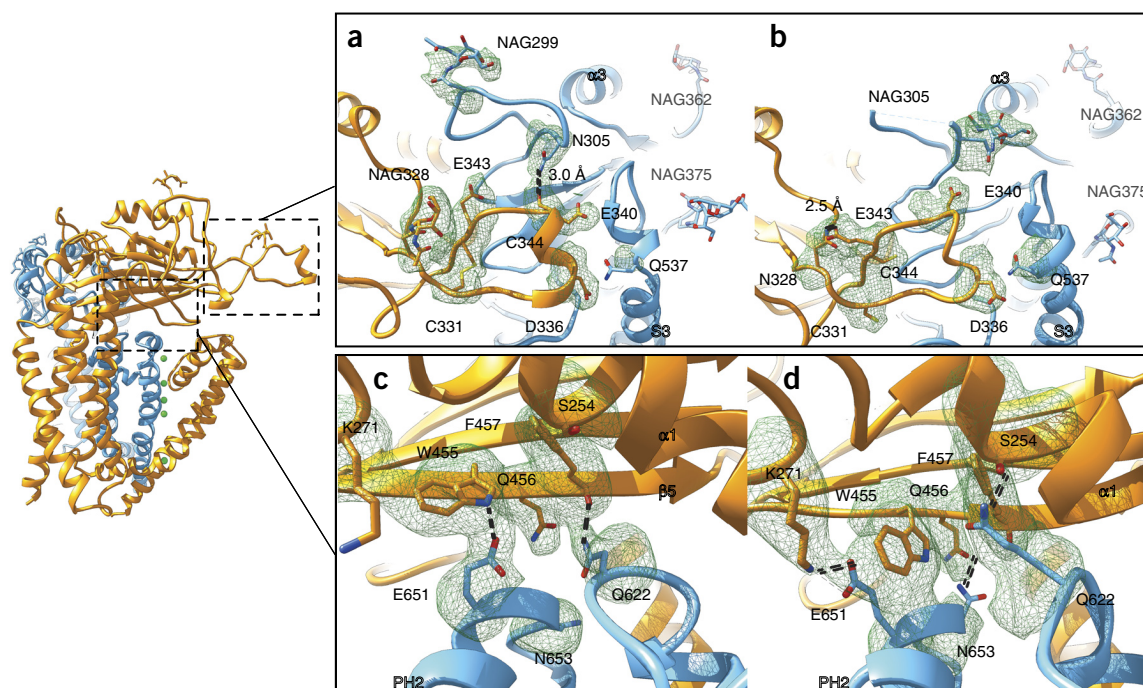
Figure 4 N-glycosylation and tetramer interactions of $PC2_{MI}$ and $PC2_{SI}$. (**a**) N-glycosylation pattern and disulfide bridge in $PC2_{MI}$. (**b**) View of $PC2_{SI}$ in the same location as in **a**. Key residues are shown as sticks with map densities (mesh at 2.5σ). (**c,d**) Conformational changes in the extracellular-domain-switching interactions with residues in the P loop of $PC2_{MI}$ (**c**) and in $PC2_{SI}$ (**d**). Key residues are shown as sticks with map densities (mesh at 2.5σ). Interactions are shown as broken black lines. Left, overview of the $PC2_{MI}$ protomer indicating the positions of detailed views in **a–d**.

leaflet, and a third (FA3) belongs to the cytoplasmic leaflet. Cholesteryl hemisuccinate (CHS), which was added during purification, fits two more compact densities. A continuous density sufficiently large to accommodate a phospholipid molecule is present at the junction of S4 with EL3, β5 and S6 of the adjacent protomer. In both maps, the space and head-group coordination by surrounding positive residues supports phosphatidic acid (PA) binding. Other negatively charged head groups, for example, phosphatidylinositol (PI) or phosphatidylglycerol, would not fit. The observed relative positions of the lipids and fatty acids are similar to those observed in the recent structure of TRPV1 in lipid nanodiscs[39] (**Fig. 5b**).

The PA lipid interacts extensively with the TOP domain in $PC2_{SI}$. His379 and Trp380 in EL3, Gln456 and Arg440 in the partly unfolded β5, and Asn653 in the P loop interact with the phosphate group of PA (**Fig. 5d**). This binding site is specific to $PC2_{SI}$, whereas in $PC2_{MI}$ the PA is less tightly coordinated (**Fig. 5c**). The extended conformation of EL3 in this form shifts His379 out of range for tight head-group coordination, and only Gln557 in S4 interacts with the PA glycerol backbone. The TOP domain and P loop are not involved in lipid interactions in $PC2_{MI}$.

Phe634 in PH1 and Phe666 in S6 coordinate FA1 in the two PC2 structures. Gln630 interacts with FA2 and FA1 in both states, although at slightly different positions. In $PC2_{MI}$, Phe605 interacts with FA2, whereas in $PC2_{SI}$ Phe605 reorients, and FA2 is displaced (**Supplementary Fig. 6a,b**). FA3 is located in the cytoplasmic leaflet coordinated by Phe567, Ile571 and Phe574 in S4 and Phe667 in S6 of the adjacent protomer (**Fig. 5f** and **Supplementary Fig. 6a,b**).

Changes in the fatty acid coordination between the two open states are related to a bulky density close to S1 and S4 at the cytoplasmic side of $PC2_{SI}$ (**Fig. 5e** and **Supplementary Fig. 6c,d**). This density, which is absent in $PC2_{MI}$, would accommodate the EF-hand motif of the C-terminal domain, which contains the Ca^{2+}-binding site (**Fig. 5f**

and **Supplementary Fig. 6d**). Arg581 in the loop between S4 and the S4–S5 linker helix might provide an interaction partner for negatively charged residues in α4 of the EF hand. The S4–S5 linker loop has a different conformation in $PC2_{MI}$, thus accounting for changes in the coordination of Asp511. The D511V mutation has been shown to cause loss of channel function in PC2, and it is a well-characterized mutation found in people with ADPKD[2,11,21]. In $PC2_{SI}$, Asp511 is coordinated by Lys575, whereas it interacts with Lys572 after conformational changes in S4 in $PC2_{MI}$. A more detailed discussion of the structural effects of this and other ADPKD sequence variants can be found in Grieben *et al.*[29].

DISCUSSION

PC2 is a Ca^{2+}-dependent, Ca^{2+}-permeable nonselective cation channel[8]. Ca^{2+} binding to the C-terminal EF hand is thought to gate PC2 activation occurring at cytosolic Ca^{2+} concentrations in the nanomolar-to-micromolar range. We observed cations in only the ion-translocation pathway of the full-length PC2 structures with the EF-hand motif, whereas $PC2_{CL}$ is missing the Ca^{2+}-sensing EF-hand motif and is not in complex with ions. We assume that the different channel conformations in the three structures (**Supplementary Videos 1** and **2**) might reflect different activation states.

PC2 has also been suggested to be a Ca^{2+} leak channel whose conductance depends on the Ca^{2+} concentration gradient and the permeability and/or selectivity for Ca^{2+} over other cations. A 'multi-ion mode' similar to that of $PC2_{MI}$ has recently been observed in TRPV6 (ref. 35), which is selective for exclusively Ca^{2+}. Therefore, we propose that $PC2_{MI}$ is a Ca^{2+}-blocked state. Ca^{2+} binding to the highly coordinated Ca1 site (**Fig. 3c**) might block monovalent cation currents[40,41], a result in good agreement with the inactivation of the channel at high Ca^{2+} concentrations[30]. The downstream cation sites (Cat2–Cat4) would allow for stepwise binding with relatively low chemical
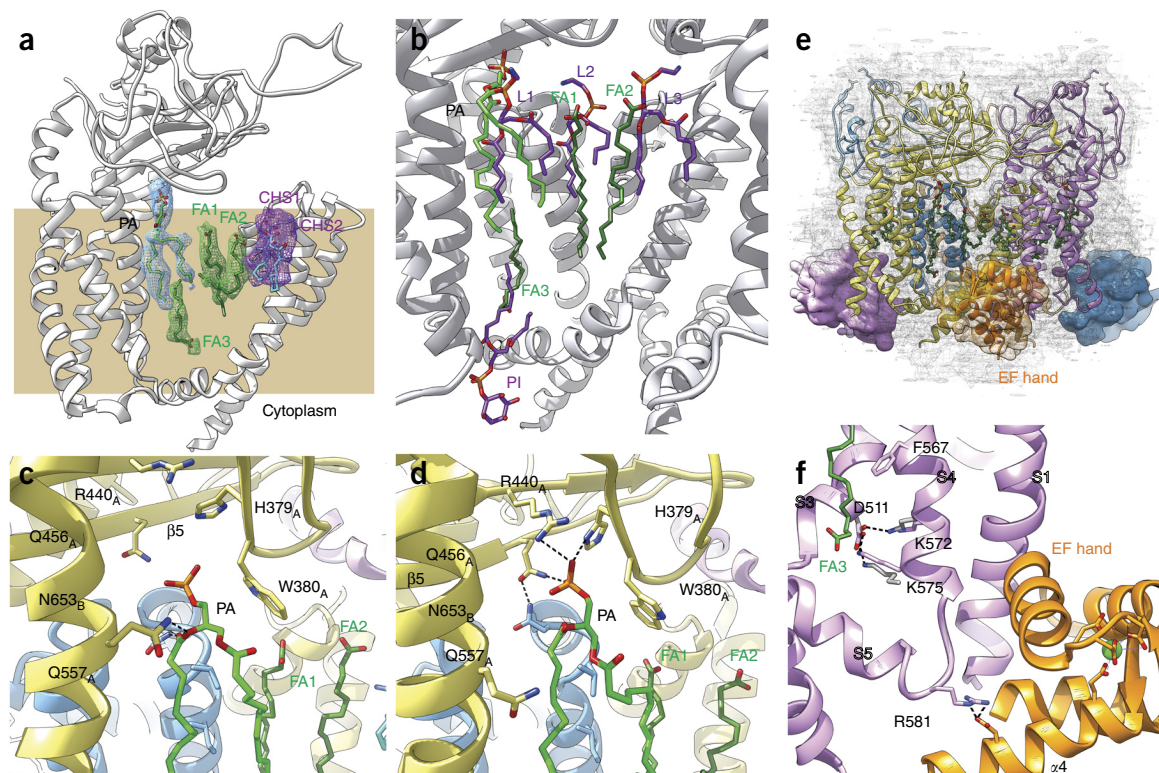
Figure 5 Lipid and fatty acid coordination in PC2. (**a**) Nonprotein density (blue) in PC2$_{MI}$ and in PC2$_{SI}$ is assigned to phosphatidic acid (PA, light-green stick models) in the hydrophobic cleft formed by S3–S6 of one protomer and S5 and S6 of the adjacent protomer. Three elongated densities (green mesh in **a**) are assigned to single-chain saturated 16:0 palmitic acids; two compact densities (purple mesh in **a**) are assigned to cholesteryl hemisuccinate (CHS; purple). (**b**) Surroundings of PA and FA1–FA3 superposed on lipid positions in the structure of TRPV1 (PDB 5IRZ). Lipids and phosphatidylinositol (L1–L3 and PI) bound to TRPV1 are shown as purple sticks, with PI in the cytoplasmic leaflet. (**c**,**d**) Coordination of PA in PC2$_{MI}$ (**c**) and PC2$_{SI}$ (**d**). (**e**) Densities attributed to the C-terminal domains of the respective protomer are shown as volumes. Fitted structure of an EF hand (orange ribbon; PDB 2Y4Q) is indicated. FA2 bends around this density. Total density is shown as gray mesh. (**f**) Close-up view of the proposed interaction of the EF hand and R581 in the S4–S5 linker of PC2$_{SI}$ (magenta). The interaction of D511 with K575 and K572 in PC2$_{SI}$ (magenta) and PC2$_{MI}$ (gray) differs substantially, and the conformation of R581 is different.

potential-energy barriers between them, thus increasing conductance through a knockoff mechanism. At higher Ca^{2+} concentrations, the stronger charge of the divalent Ca^{2+} ions might modulate conductance and selectivity for Ca^{2+} over monovalent ions. Ca^{2+} might block the preselectivity filter as well, possibly as part of a Ca^{2+}-mediated regulatory mechanism. In PC2$_{SI}$, in which the Ca^{2+}-sensing C-terminal EF-hand motif is observed, the preselectivity and selectivity filters are clearly more open.

In PC2$_{MI}$, the vestibule entrance is restricted at the Cat0 site (**Figs. 2a,d** and **3c**) and would prevent the efflux of stripped water in this pathway. An amphipathic funnel extends from a position above the selectivity filter to the hydrophobic cavity that accommodates the PA lipid and the fatty acids (**Fig. 2d**). This funnel might serve as a water pathway that affects the hydration states of the vestibule. It appears that the selectivity filter remains blocked as long as the excess of water is not removed from the ion-translocation pore. Gln630 as well as FA1, which is located at a position relatively similar to that of a phosphatidylcholine lipid in TRPV1 (ref. 39), restrict the funnel exit, thus suggesting a role of lipids in this potential conductance regulation (**Fig. 6**). In PC2$_{SI}$, the entrance gate of the vestibule is more open, and a fatty acid entirely blocks the funnel exit (**Fig. 2e**).

Lipids have also been found in TRPV1 (ref. 39) and contribute to its activation mechanism. However, lipid specificity and coordination in the two TRP channels is very different. In TRPV1, a PI binds in the same position in the cytoplasmic membrane leaflet as that of FA3

in PC2. Whereas FA3 interacts primarily with S4, PI is a competitive vanilloid antagonist of TRPV1, and it affects the orientation the S4–S5 linker and stabilizes the resting state[39]. Both open PC2 structures differ from each other and from the closed state at the S4–S5 linker (**Fig. 1e** and **Supplementary Fig. 5c,d**). In PC2$_{SI}$, the S4–S5 linker probably interacts with residues in α4 in the EF hand (**Fig. 5e,f**), thus causing a conformational change at the lower gates that is reminiscent of that in vanilloid-agonist binding in TRPV1 (ref. 39). A salt bridge between an arginine in S4 and a glutamate in S5 is formed in the open state of TRPV1. We did not observe a similar interaction at this exact position in PC2, but the interaction between Asp511 in S3 with Lys572 or Lys575 in S4 might stabilize the open conformation of the lower gates (**Fig. 5f**).

In the exoplasmic leaflet, the phosphatidylcholine lipids bound to TRPV1 are loosely coordinated, whereas PA at the same position in PC2 forms a tight tripartite complex with the P loop and the TOP domain (**Fig. 5c,d**). In TRPV1, docking of the DkTx toxin is supported by lipid interactions, and its binding opens the upper gates. In PC2, a stretch of EL3 from the fifth N-glycosylation site, Asn375, which is present in only human PC2 (ref. 23), up to Gly390, enters the hydrophobic cavity. This region of the TOP domain, together with the PA lipid might be involved in stabilizing the open PC2$_{SI}$ state. The PA–TOP domain complex establishes the more extended P-loop conformation in PC2$_{SI}$ (**Fig. 4d**) and ultimately triggers opening of the selectivity filter. We did not add PA during purification, and given
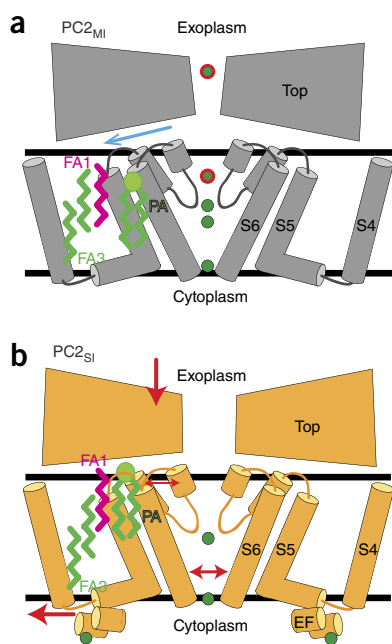
Figure 6 Schematic representation of the multi-ion mode of $PC2_{MI}$ and single-ion mode of $PC2_{SI}$. (**a**) Conductance regulation of cations (green spheres) might be achieved by Ca^{2+} (circled red) blocking in the selectivity and preselectivity filter (TOP), thus leading to water accumulation in the amphipathic funnel (blue arrow). (**b**) In $PC2_{SI}$, lipid-mediated interactions of C-terminal and TOP domains induce further opening of the upper and lower gates through the formation of a tripartite complex. FA1 (magenta) blocks the amphipathic funnel. Red arrows indicate the relative conformational differences between $PC2_{SI}$ and $PC2_{MI}$.

that it is the main precursor for lipid biosynthesis, PA was present only at low steady-state levels in the ER. Its removal from the biosynthetic equilibrium by high levels of PC2 would therefore affect the ER lipid pool in many ways. PA is also known to affect membrane curvature. Depletion of PA plus a potential subsequent upregulation of PA biosynthesis would be expected to affect the shape and extent of the ER, thus resulting in crystalloid formation.

The role of lipids in PC2 activation is not confirmed by functional data, but our maps indicate that the type of lipid may be crucial for the conformation of the selectivity filter, owing to the lipid-mediated interaction between the P loop and TOP domain. The positively charged groove of the PA-binding site might potentially also accommodate other negatively charged lipids, if the orientation of the TOP domain orientation were to change slightly. A bulkier lipid such as PI would push the TOP domain away from the membrane and hence might change the selectivity or activation mode in PC2. The preferred locations of PC2 outside the ER, such as the ciliary membrane or the plasma membrane, differ in the content of negatively charged lipids. For example, the ciliary membrane contains elevated levels of phosphoinositides and sterols. The differences in lipid composition may directly contribute to the functional diversity of PC2 at different locations.

The two open states of PC2 provide insights into a regulatory action of Ca^{2+} in modulating cation currents. The conserved lipid-binding sites in PC2 provide a preliminary glimpse of a potential lipid-mediated activation mechanism that also involves the TOP and C-terminal domains. The binding of different membrane lipids would help to partially explain the location-dependent functional diversity reported for PC2. Together, the structures of PC2 in open and closed conformations provide a wealth

of new information not only on the structural effects of ADPKD mutations but also on how PC2 interacts with ions and lipids and how these interactions affect the conformations of the channel, thereby potentially providing mechanisms underlying regulation of the channel.

METHODS

Methods, including statements of data availability and any associated accession codes and references, are available in the online version of the paper.

Note: Any Supplementary Information and Source Data files are available in the online version of the paper.

AUTHOR CONTRIBUTIONS

C.Z. directed research; M.W. performed cloning, established the expression systems, and collected and processed cryo-EM data; M.W., L.K., R.M.R. and S.R. expressed and purified PC2; D.R. performed FIB-SEM tomography; F.J. carried out freeze fracture, thin sectioning and immunogold labeling; M.W. and V.H. performed negative-stain single-particle analysis; M.G.M. and S.D.S. carried out homology modeling; M.G., A.C.W.P., J.T.H. and E.P.C. contributed the structure of the closed conformation of PC2; M.G.M. and C.Z. performed structure determination and refinement and analyzed the data; and M.G.M., W.K., M.W., R.W., E.P.C. and C.Z. wrote the manuscript.

1. Petersen, O.H., Michalak, M. & Verkhratsky, A. Calcium signalling: past, present and future. *Cell Calcium* **38**, 161–169 (2005).
2. Mochizuki, T. *et al.* PKD2, a gene for polycystic kidney disease that encodes an integral membrane protein. *Science* **272**, 1339–1342 (1996).
3. Kim, S. *et al.* The polycystin complex mediates Wnt/Ca²⁺ signalling. *Nat. Cell Biol.* **18**, 752–764 (2016).
4. Giamarchi, A. *et al.* A polycystin-2 (TRPP2) dimerization domain essential for the function of heteromeric polycystin complexes. *EMBO J.* **29**, 1176–1191 (2010).
5. Cai, Y. *et al.* Identification and characterization of polycystin-2, the PKD2 gene product. *J. Biol. Chem.* **274**, 28557–28565 (1999).
6. Köttgen, M. *et al.* Trafficking of TRPP2 by PACS proteins represents a novel mechanism of ion channel regulation. *EMBO J.* **24**, 705–716 (2005).
7. Gallagher, A.R. *et al.* A truncated polycystin-2 protein causes polycystic kidney disease and retinal degeneration in transgenic rats. *J. Am. Soc. Nephrol.* **17**, 2719–2730 (2006).
8. González-Perrett, S. *et al.* Polycystin-2, the protein mutated in autosomal dominant polycystic kidney disease (ADPKD), is a Ca²⁺-permeable nonselective cation channel. *Proc. Natl. Acad. Sci. USA* **98**, 1182–1187 (2001).
9. Luo, Y., Vassilev, P.M., Li, X., Kawanabe, Y. & Zhou, J. Native polycystin 2 functions as a plasma membrane Ca²⁺-permeable cation channel in renal epithelia. *Mol. Cell. Biol.* **23**, 2600–2607 (2003).
10. Vassilev, P.M. *et al.* Polycystin-2 is a novel cation channel implicated in defective intracellular Ca²⁺ homeostasis in polycystic kidney disease. *Biochem. Biophys. Res. Commun.* **282**, 341–350 (2001).

11. Koulen, P. *et al.* Polycystin-2 is an intracellular calcium release channel. *Nat. Cell Biol.* **4**, 191–197 (2002).
12. Anyatonwu, G.I., Estrada, M., Tian, X., Somlo, S. & Ehrlich, B.E. Regulation of ryanodine receptor-dependent calcium signaling by polycystin-2. *Proc. Natl. Acad. Sci. USA* **104**, 6454–6459 (2007).
13. Li, Y., Wright, J.M., Qian, F., Germino, G.G. & Guggino, W.B. Polycystin 2 interacts with type I inositol 1,4,5-trisphosphate receptor to modulate intracellular Ca^{2+} signaling. *J. Biol. Chem.* **280**, 41298–41306 (2005).
14. Tsiokas, L. *et al.* Specific association of the gene product of PKD2 with the TRPC1 channel. *Proc. Natl. Acad. Sci. USA* **96**, 3934–3939 (1999).
15. Sukumaran, P., Schaar, A., Sun, Y. & Singh, B.B. Functional role of TRP channels in modulating ER stress and autophagy. *Cell Calcium* **60**, 123–132 (2016).
16. Köttgen, M. *et al.* TRPP2 and TRPV4 form a polymodal sensory channel complex. *J. Cell Biol.* **182**, 437–447 (2008).
17. Zhang, P. *et al.* The multimeric structure of polycystin-2 (TRPP2): structural-functional correlates of homo- and hetero-multimers with TRPC1. *Hum. Mol. Genet.* **18**, 1238–1251 (2009).
18. Tsiokas, L., Kim, E., Arnould, T., Sukhatme, V.P. & Walz, G. Homo- and heterodimeric interactions between the gene products of PKD1 and PKD2. *Proc. Natl. Acad. Sci. USA* **94**, 6965–6970 (1997).
19. Qian, F. *et al.* PKD1 interacts with PKD2 through a probable coiled-coil domain. *Nat. Genet.* **16**, 179–183 (1997).
20. Chauvet, V. *et al.* Mechanical stimuli induce cleavage and nuclear translocation of the polycystin-1 C terminus. *J. Clin. Invest.* **114**, 1433–1443 (2004).
21. Wilson, P.D. Polycystic kidney disease. *N. Engl. J. Med.* **350**, 151–164 (2004).
22. Geng, L. *et al.* Polycystin-2 traffics to cilia independently of polycystin-1 by using an N-terminal RVxP motif. *J. Cell Sci.* **119**, 1383–1395 (2006).
23. Hofherr, A., Wagner, C., Fedeles, S., Somlo, S. & Köttgen, M. N-glycosylation determines the abundance of the transient receptor potential channel TRPP2. *J. Biol. Chem.* **289**, 14854–14867 (2014).
24. Yang, Y. & Ehrlich, B.E. Structural studies of the C-terminal tail of polycystin-2 (PC2) reveal insights into the mechanisms used for the functional regulation of PC2. *J. Physiol. (Lond.)* **594**, 4141–4149 (2016).
25. Yu, Y. *et al.* Structural and molecular basis of the assembly of the TRPP2/PKD1 complex. *Proc. Natl. Acad. Sci. USA* **106**, 11558–11563 (2009).
26. Hanaoka, K. *et al.* Co-assembly of polycystin-1 and -2 produces unique cation-permeable currents. *Nature* **408**, 990–994 (2000).
27. Cai, Y. *et al.* Calcium dependence of polycystin-2 channel activity is modulated by phosphorylation at Ser812. *J. Biol. Chem.* **279**, 19987–19995 (2004).
28. Arif Pavel, M. *et al.* Function and regulation of TRPP2 ion channel revealed by a gain-of-function mutant. *Proc. Natl. Acad. Sci. USA* **113**, E2363–E2372 (2016).
29. Grieben, M. *et al.* Structure of the polycystic kidney disease TRP channel Polycystin-2 (PC2). *Nat. Struct. Mol. Biol.* http://dx.doi.org/10.1038/nsmb.3343 (2016).
30. Shen, P.S. *et al.* The structure of the polycystic kidney disease channel PKD2 in lipid nanodiscs. *Cell* **167**, 763–773 e11 (2016).
31. Reeves, P.J., Callewaert, N., Contreras, R. & Khorana, H.G. Structure and function in rhodopsin: high-level expression of rhodopsin with restricted and homogeneous N-glycosylation by a tetracycline-inducible N-acetylglucosaminyltransferase I-negative HEK293S stable mammalian cell line. *Proc. Natl. Acad. Sci. USA* **99**, 13419–13424 (2002).
32. Narayan, K. & Subramaniam, S. Focused ion beams in biology. *Nat. Methods* **12**, 1021–1031 (2015).
33. Liao, M., Cao, E., Julius, D. & Cheng, Y. Structure of the TRPV1 ion channel determined by electron cryo-microscopy. *Nature* **504**, 107–112 (2013).
34. Paulsen, C.E., Armache, J.P., Gao, Y., Cheng, Y. & Julius, D. Structure of the TRPA1 ion channel suggests regulatory mechanisms. *Nature* **520**, 511–517 (2015).
35. Saotome, K., Singh, A.K., Yelshanskaya, M.V. & Sobolevsky, A.I. Crystal structure of the epithelial calcium channel TRPV6. *Nature* **534**, 506–511 (2016).
36. Zwart, P.H. *et al.* Automated structure solution with the PHENIX suite. *Methods Mol. Biol.* **426**, 419–435 (2008).
37. Lyskov, S. *et al.* Serverification of molecular modeling applications: the Rosetta Online Server that Includes Everyone (ROSIE). *PLoS One* **8**, e63906 (2013).
38. Tang, L. *et al.* Structural basis for Ca^{2+} selectivity of a voltage-gated calcium channel. *Nature* **505**, 56–61 (2014).
39. Gao, Y., Cao, E., Julius, D. & Cheng, Y. TRPV1 structures in nanodiscs reveal mechanisms of ligand and lipid action. *Nature* **534**, 347–351 (2016).
40. Catterall, W.A. Voltage-gated calcium channels. *Cold Spring Harb. Perspect. Biol.* **3**, a003947 (2011).
41. Parnas, M., Katz, B. & Minke, B. Open channel block by Ca^{2+} underlies the voltage dependence of *Drosophila* TRPL channel. *J. Gen. Physiol.* **129**, 17–28 (2007).

ONLINE METHODS

Cloning, expression and protein production. The human *PKD2* gene with a StrepII-tag fused to the C terminus was cloned into the pACMV-tetO vector[31,42] via the restriction sites KpnI and XhoI. Transfection of eukaryotic cells and selection in the cell line HEK293S GnTI⁻ was performed in six-well tissue culture plates in DMEM/Ham's F12 medium with 10% FBS, 50 U/ml pen/strep and 5 µg/ml blasticidin at 37 °C and 5% CO_2. HEK293S GnTI⁻ cells were tested for mycoplasma contamination.

For selection of a stable HEK293S GnTI⁻ cell line, 350 µg gentamycin was added into DMEM/Ham's F12 medium with 10% FBS, 50 U/ml pen/strep and 5 µg/ml blasticidin. Single cells were transferred into 96-well tissue culture plates. Test expression assays were performed in six-well plates, whereas expression for protein purification was performed in suspension with volumes up to 4 l. Expression was induced with the final addition of medium containing tetracycline and sodium butyrate to a final concentration of 3 µg/ml and 5 mM, respectively. 48 h after induction, cells were harvested by centrifugation (25 min, 3,600*g* at 4 °C). Cells were resuspended in PBS buffer and centrifuged again for 10 min at 4,500*g* and 4 °C. The cell pellet was resuspended in buffer (25 mM HEPES, pH 7.5, 10% glycerol, 150 mM NaCl, 2 mM $CaCl_2$ and complete protease inhibitor) for cell disruption. Cells were lysed with a cell disruptor (Constant Systems) at 2.0 kbar and 4 °C. Cell debris was removed by centrifugation for 15 min at 10,000*g* and 4 °C, and membranes were sedimented at 150,000*g*, 4 °C for 60 min, resuspended in 10–50 ml buffer (25 mM HEPES, pH 7.5, 10% glycerol, 150 mM NaCl and 2.5 mM $CaCl_2$) and homogenized with a Dounce homogenizer. The total protein concentration was adjusted to 2.5 mg/ml, and samples were stirred while detergent was slowly added to a final concentration of 1%:0.4% LMNG/CHS (w/w). PC2 was purified with Strep-Tactin Sepharose (IBA). Proteins were eluted with 5 mM desthiobiotin. Amphipol A8-35 was added to the purified PC2 in a three-fold excess (w/w), and the mixture was incubated at 4 °C for 4 h. 15 mg of activated biobeads was added per 1 ml protein–detergent–amphipol mixture and incubated overnight at 4 °C. Biobeads were removed with a plastic column. PC2 was concentrated with Vivaspin 4 (Sartorius) centrifugal filter units with a molecular-weight cutoff of 100 kDa, to a final volume of 50 µl. Size-exclusion chromatography was performed on an Ettan system (GE Healthcare) with Superose 6 3.2/300, and absorption was measured at 280 nm.

Electron cryomicroscopy. For cryo-EM, PC2 in amphipol A8-35 was concentrated to 1 mg/ml, and aliquots of 3 µl were placed on glow-discharged holey carbon grids (Quantifoil R2/2) and plunge-frozen with a Vitrobot IV (FEI) at 100% humidity, 10 °C with a 9-s blotting time. Cryo-EM images were collected at liquid-nitrogen temperature on a JEOL 3200 FSC electron microscope operating at 300 kV with an in-column energy filter and equipped with a K2 Summit direct electron-detector camera (Gatan). The slit width was adjusted to 20 eV, and images were recorded in counting mode at a nominal magnification of 30,000×, corresponding to a pixel size of 1.14 Å on the specimen. The total exposure time was 7 s, thus leading to an accumulated dose of 55 e⁻/Å². Each image was fractionated into 35 subframes with an accumulation time of 0.2 s. Defocus values in the final data sets ranged from 0.5 to 4.0 µm.

Image processing. Global beam-induced motion of images was corrected with MOTIONCORR 2.0 (ref. 43) and then with Unblur[44–46]. The contrast transfer function for each image was determined with CTFFIND3 (ref. 47). An initial set of 25,000 particles were picked manually and subjected to 2D class averaging. The six most representative 2D class averages were filtered to 20 Å and used as templates for reference-based particle picking[48]. Each micrograph was manually inspected, false-positive particles were deleted, and false-negative particles were selected, thus yielding a total of 267,010 particles from 1,450 micrographs. Subsequent 2D and 3D classifications were performed with RELION-1.4 (ref. 49). A 3D classification without symmetry was initially imposed with the TRPV1 channel (PDB 3J5P)[33] filtered to 60 Å as a reference, and a sampling of 15° resulted in a subset of 162,074 particles. In subsequent 3D classification, the best 3D class average of the first classification was used as a starting model, the sampling was set to 7.5°, and *C*4 symmetry was imposed. This process yielded a subset of 108,240 particles, which were analyzed by 2D class averaging with 'ignore first peak' in the RELION-1.4 GUI[49]. The same particle subset was used for a 3D gold-standard refinement[50], thus resulting in a resolution of 4.2 Å. Particle-based beam-induced movement correction and polishing were performed[51,52] with a running average

of seven movie frames and an s.d. of one pixel for the translational alignments, thus yielding a reconstruction with a resolution of 3.9 Å. A subsequent 3D classification with a sampling rate of 7.5° and *C*4 symmetry imposed separated two different conformations of PC2. The two conformations were refined separately, thereby resulting in two different cryo-EM structures with resolutions of 4.2 Å and 4.3 Å, respectively. Densities were sharpened by the application of *B* factors[53] estimated with RELION-1.4 (ref. 49). Local resolutions in different parts of the maps were estimated with RESMAP[54]. Densities were visualized, and atomic models were fitted in cryo-EM densities with UCSF Chimera[55].

Model building for the S1–S4 and pore domains. Template structures homologous to the target sequence were initially detected by iterative HMM–HMM comparison (HHblits) and chosen on the basis of their amino acid sequence identity and similarity. Initial alignment was obtained in an automated manner with AlignMe[56]. MODELLER[57] was then used for comparative structure modeling to obtain an initial model. TRPA1 (PDB 3J9P) served as the template for S1 and S3–S5, TRPV1 (PDB 3J5Q) served as the template for S5 and S6, and TRPV2 (PDB 5AN8) fitted best for S2 and S3. After manual correction of the sequence-to-sequence alignment, the final model was obtained from FLEX-EM (http://topf-group.ismb.lon.ac.uk/flex-em/). The FLEX-EM model was investigated with EMRinger[58] and subjected to iterative runs of refinement with the Rosetta tool[46,59] for structure determination in cryo-EM density and Phenix real-space-refinement[45,60]. Regions that that could not be modeled on the basis of homology were either manually corrected or built *de novo* with COOT[44].

Purification of crystalloid ER membranes. The HEK293S GnTI⁻ cell line stably expressing PKD2 was cultured in T175 tissue culture plates until 70% confluence was reached, and protein production was induced by the addition of 3 µg/ml tetracycline and 5 mM sodium butyrate. Cells were harvested by centrifugation for 10 min at 4,500*g* and 4 °C and resuspended in 3 ml of ice-cold 40 mM HEPES, pH 7.2, 5 mM $MgCl_2$, 5 mM EGTA, complete protease inhibitor and DNase. Cells were passaged 35 times through a 27-gauge needle in 1-ml batches on ice. Cell debris was sedimented at 1,000*g* and 4 °C for 10 min. Cell pellets were resuspended in buffer without DNase and centrifuged again. The cell pellet was then resuspended in buffer containing 2.2 M sucrose, and a continuous sucrose gradient (1.5–0.7 M sucrose in 40 mM HEPES, pH 7.2, 5 mM $MgCl_2$, 5 mM EGTA and complete protease inhibitor) was added on top. Membranes were separated by centrifugation for 20 h at 40,000*g* at 4 °C. The gradient was separated in 1-ml fractions, and the fraction that contained the highest amount of PC2 (as determined by SDS–PAGE) was used for freeze-fracture labeling.

Immunolabeling of thin sections. The stable cell line was cultured in six-well tissue culture plates until 70% confluence was reached, and protein production was induced by the addition of 3 µg/ml tetracycline and 5 mM sodium butyrate. Cells or purified crystalloid ER were fixed for 2 h at room temperature with 2% (v/v) paraformaldehyde in PBS buffer. The samples were washed three times with PBS buffer for 10 min and incubated with 2% glycine in PBS buffer for 2.5 h at room temperature before being washed again three times with PBS buffer. The samples were embedded in 4% Bacto Agar (BD), dehydrated with an ethanol-gradient series (1 × 20 min at 30%, 2 × 20 min at 50%, 2 × 30 min at 70%, 2 × 30 min at 90% and 2 × 30 min at 100%) and infiltrated with LR white medium-grade acrylic resin (Resin Company). Polymerization was carried out at 55 °C for 36 h, and 80- to 120-nm thin sections were prepared with an Ultracut S Microtome (Leica). The thin sections were incubated with saturated sodium periodate for 1 h at room temperature. The sample was washed five times (1 × 10 min with 2% glycine in PBS buffer, 1 × 10 min with PBS buffer, 1 × 10 min with 1% BSA in PBS buffer containing 0.1% Tween 20, 2 × 10 min with 0.1% BSA in PBS buffer and 0.1% Tween 20) before anti-PC2 antibody (YCE2, Santa Cruz Biotechnology, cat. no. sc-47734; validation provided on the manufacturer's website) in PBS buffer with 0.1% BSA was added and incubated for 1 h. The primary antibody was removed, and four washes with PBS were carried out for 5 min each, before the secondary antibody (anti-mouse coupled to 18-nm gold, Thermo Fisher Scientific, cat. no. N-24915) in PBS buffer with 0.1% BSA was added and incubated for 1 h. Free antibody was removed by washing the sample three times for 5 min with PBS buffer. Then 1% (v/v) glutaraldehyde in PBS was added and incubated for 10 min, and the sample was washed three times with ddH₂O and stained with 1% (w/v) uranyl acetate and lead citrate. Samples were analyzed with an EM208S electron microscope (FEI).

FIB-SEM. The stable cell line was cultured in six-well tissue culture plates until 70% confluence was reached, and protein production was induced by the addition of 3 μg/ml tetracycline and 5 mM sodium butyrate. The medium was removed, and 2.5% (v/v) glutaraldehyde in 100 mM sodium cacodylate, pH 7.4, was used to prefix cells or purified crystalloid ER for 2 h at room temperature. Prefixed samples were washed three times with 100 mM sodium cacodylate, pH 7.2, for 15 min, scraped and subsequently embedded in 4% Bacto Agar (BD). Samples were dehydrated with an ethanol-gradient series (1×20 min at 30%, 2×20 min at 50%, 2×30 min at 70%, 2×30 min at 90% and 2×30 min at 100%) and infiltrated with Low Viscosity Premix Kit Medium (2×20 min at 30%, 2×30 min at 50%, 2×30 min at 75%, overnight at 100%, and 2×2 h at 100%) (Agar Scientific). Polymerization was performed for 16 h at 60 °C. For FIB-SEM, resin blocks were trimmed with a glass knife to expose the cells, and the blocks were glued to SEM stubs with silver paint. Gold was sputtered onto the sample to minimize electrostatic charging. Samples were analyzed in a Zeiss Auriga FIB-SEM at an acceleration voltage of 10 kV to localize embedded cells. An additional platinum layer was deposited with a gas-injection system. A 30-kV gallium beam was used to prepare a block face, which was subsequently analyzed by FIB-SEM tomography at an acceleration voltage of 1.8 kV. A 600-pA Ga$^+$ beam was used to abrade the block face and to collect a 3D data set. The slice thickness was 10 nm. Images were recorded with an EsB detector. Image stacks were aligned and segmented with the Amira package.

Data availability. EM density maps have been deposited in the Electron Microscopy Data Bank under accession codes EMD-3524 (PC2$_{MI}$) and EMD-3523 (PC2$_{SI}$). Atomic models have been deposited in the Protein Data Bank under accession codes PDB 5MKF (PC2$_{MI}$) and PDB 5MKE (PC2$_{SI}$). Other supporting data are available from the authors upon reasonable request.

42. Reeves, P.J., Kim, J.M. & Khorana, H.G. Structure and function in rhodopsin: a tetracycline-inducible system in stable mammalian cell lines for high-level expression of opsin mutants. *Proc. Natl. Acad. Sci. USA* **99**, 13413–13418 (2002).

43. Li, X. *et al.* Electron counting and beam-induced motion correction enable near-atomic-resolution single-particle cryo-EM. *Nat. Methods* **10**, 584–590 (2013).
44. Grant, T. & Grigorieff, N. Measuring the optimal exposure for single particle cryo-EM using a 2.6 Å reconstruction of rotavirus VP6. *eLife* **4**, e06980 (2015).
45. Campbell, M.G. *et al.* Movies of ice-embedded particles enhance resolution in electron cryo-microscopy. *Structure* **20**, 1823–1828 (2012).
46. Brilot, A.F. *et al.* Beam-induced motion of vitrified specimen on holey carbon film. *J. Struct. Biol.* **177**, 630–637 (2012).
47. Mindell, J.A. & Grigorieff, N. Accurate determination of local defocus and specimen tilt in electron microscopy. *J. Struct. Biol.* **142**, 334–347 (2003).
48. Scheres, S.H. Semi-automated selection of cryo-EM particles in RELION-1.3. *J. Struct. Biol.* **189**, 114–122 (2015).
49. Scheres, S.H. RELION: implementation of a Bayesian approach to cryo-EM structure determination. *J. Struct. Biol.* **180**, 519–530 (2012).
50. Scheres, S.H. & Chen, S. Prevention of overfitting in cryo-EM structure determination. *Nat. Methods* **9**, 853–854 (2012).
51. Scheres, S.H. Beam-induced motion correction for sub-megadalton cryo-EM particles. *eLife* **3**, e03665 (2014).
52. Bai, X.C., Fernandez, I.S., McMullan, G. & Scheres, S.H. Ribosome structures to near-atomic resolution from thirty thousand cryo-EM particles. *eLife* **2**, e00461 (2013).
53. Chen, S. *et al.* High-resolution noise substitution to measure overfitting and validate resolution in 3D structure determination by single particle electron cryomicroscopy. *Ultramicroscopy* **135**, 24–35 (2013).
54. Kucukelbir, A., Sigworth, F.J. & Tagare, H.D. Quantifying the local resolution of cryo-EM density maps. *Nat. Methods* **11**, 63–65 (2014).
55. Pettersen, E.F. *et al.* UCSF Chimera: a visualization system for exploratory research and analysis. *J. Comput. Chem.* **25**, 1605–1612 (2004).
56. Stamm, M., Staritzbichler, R., Khafizov, K. & Forrest, L.R. Alignment of helical membrane protein sequences using AlignMe. *PLoS One* **8**, e57731 (2013).
57. Webb, B. & Sali, A. Protein structure modeling with MODELLER. *Methods Mol. Biol.* **1137**, 1–15 (2014).
58. Barad, B.A. *et al.* EMRinger: side chain-directed model and map validation for 3D cryo-electron microscopy. *Nat. Methods* **12**, 943–946 (2015).
59. Song, Y. *et al.* High-resolution comparative modeling with RosettaCM. *Structure* **21**, 1735–1742 (2013).
60. Afonine, P.V. *et al.* Towards automated crystallographic structure refinement with phenix.refine. *Acta Crystallogr. D Biol. Crystallogr.* **68**, 352–367 (2012).